TRACKING MYOCARDIAL DEFORMATION USING SPATIALLY-CONSTRAINED VELOCITIES

FRANCOIS G. MEYER, R. TODD CONSTABLE
ALBERT J. SINUSAS AND JAMES S. DUNCAN
*Image Processing and Analysis Group, Dept. of Diagnostic
Radiology, Yale University, New Haven, CT 06520, USA*

Abstract. This work proposes a unified framework to track the deformation of the myocardium using velocity fields and boundary information. The deformation of the myocardium is characterized by a deforming mesh. A general framework for locally regularizing the velocity field has been developed. The tracking is modeled as an estimation problem which makes it possible to properly take into account uncertainties in the velocity and boundary measurements. The results of experiments conducted on phantom data and on *in vivo* data demonstrate the strength of the approach.

1. Introduction

The ability to analyze and quantize the internal deformation of the myocardium from a sequence of images is of fundamental importance for the diagnosis of heart disease. A deformed body can be described by its boundary, and recent efforts have been aimed at understanding the complex motion of contours and surfaces [5, 13]. However, as opposed to a rigid object, the knowledge of internal deformations is necessary to uniquely describe the state of a deformed material. A suitable measure of deformation is provided by the strain tensor, or the rate of deformation tensor [15]. With the availability of dense 3-D velocity maps, estimating the rate of deformation of the myocardium becomes possible. Recently the authors in [4, 12] have demonstrated that velocity maps in three orthogonal directions can be measured at multiple instants throughout the cardiac cycle. This new technique, termed *phase contrast cine magnetic resonance imaging*, combines phase contrast imaging methods with cardiac cine techniques.

One limitation of the description provided by velocity maps is that it does not establish the correspondence between material points over time. An immediate understanding and analysis of the deformation of the same region of the myocardium is not available from this information alone. In principle the integration of the spatial velocity yields an estimate of the position of each material point, or particle at the next instant. In practice, serious numerical difficulties can arise. The estimate of the new position of a given particle at time $t + dt$ may not correspond to the true position at this instant. Therefore the instantaneous spatial velocity at this point will not coincide with the true velocity of the particle. If we iterate this scheme again, errors in particle positions will grow rapidly in time. Another related problem stems from the fact that any noise in the velocity will be transmitted to the position estimates. These errors may also accumulate over time. The authors in [4, 12] have encountered these difficulties when tracking small isolated regions of interest in the myocardium using phase contrast MRI velocities. They have tried to correct them by forward and reverse integration in time. Establishing trajectories of the same material points from a sequence of images is an intricate problem [1]. Except for feature points or special landmarks, there is no unique way to establish the correspondence of material particles between two successive frames. Methods exploiting geometric cues such as curvature have tackled the difficult issue of non rigid correspondence for curves [5] and surfaces [13]. Tissue tagging with MRI makes it possible to embed in the image a large number of material landmarks. These non invasive landmarks move along with the tissue as if they were implanted in the tissue. However, one severe limitation of this imaging technique is the decay of the tagging grid over the heart cycle. Establishing correspondence of these points between different images makes it possible to recover a sparse set of trajectories [7]. Another limitation is the limited transmural resolution of the tags. Most effort in the field of non-rigid motion analysis has been expended to understand the deformation of curves and surfaces [1]. However, we believe that such a description remains incomplete. We advocate therefore a continuum approach that uses velocity fields to describe the internal twisting and stretching of a deforming body.

The major contribution of this work is to explore and propose a unified framework that exploits velocity fields and boundary information to track non-rigid motion. The idea of exploiting velocity and shape information has been previously proposed in [10] in the context of the tracking of a rigid object, and we intend to merge this with the work described in [5] to estimate non-rigid motion. The approach makes it possible to track and analyze the temporal variation of stretching and twisting of any region inside the myocardium. This method should provide a powerful tool for the diagnosis

of local abnormalities in the thickening of the myocardium. We emphasize the case where velocity measurements are obtained by phase-contrast MRI, although we note that velocities can be directly estimated from the spatiotemporal changes of the intensity function [14]. The tracking is modeled as an estimation problem which makes it possible to properly take into account uncertainties in the velocity and boundary measurements. Stochastic optimal linear estimation techniques yield a solution of the estimation problem. Experiments have been conducted with real data. Encouraging results demonstrate the strength of our approach.

The paper is organized as follows. In the next section we explain how the physical assumption of local homogeneity of the rate of deformation yields an affine model of the velocity field. It is finally shown that the continuous deformation of the myocardium can be described by the positions and velocities of the vertices of a deforming mesh. The measurement algorithms that give the position and the velocity of each node of the mesh are given in Section 3. The dynamic model that describes the evolution of the deforming mesh, and the associated Kalman filter are presented in Section 4. Results of experiments conducted on real data are given in Section 5.

2. Representation of the myocardium

We represent each slice of myocardium that is imaged as a continuous medium. To construct a satisfactory description we subdivide the domain into elementary cells. We use triangles in 2-D and tetrahedra in 3-D. The deformation in each cell will characterize the continuum deformation of the body in this neighborhood. We characterize now the velocity field inside each cell.

2.1. DEFORMATION AND VELOCITY MODEL

Before describing the work any further we need to introduce a few concepts from continuum mechanics [15] . Let us consider a deformable body $\mathcal{B}$ in motion ($\mathcal{B}$ is an open set of $\mathbb{R}^3$). A motion of the body is defined as a mapping from $\mathcal{B}$ to $\mathbb{R}^3$

$$\begin{aligned} \mathcal{B} \times \mathbb{R}+ &\longrightarrow \mathbb{R}^3 \\ (\mathbf{X}, t) &\longrightarrow \mathbf{x}(\mathbf{X}, T) \end{aligned}$$

Informally we can think of $\mathbf{X}$ as being the label of a given particle, and $\mathbf{x}$ the position of this particle at time t. We can define the velocity of the particle $\mathbf{X}$ at time t as

$$\mathbf{v}(\mathbf{X}, t) = \frac{\partial \mathbf{x}}{\partial t}(\mathbf{X}, t)$$

In the continuum mechanics literature, $\mathbf{v}(\mathbf{X}, t)$ is called the material, or Lagrangian, velocity. Further we define $\mathbf{u}(\mathbf{x}, t) = (u(x, y, t), v(x, y, t))$ the Eulerian, or spatial velocity, as being the velocity of the particle that occupies the position $\mathbf{x}$ at time t. We have $\mathbf{u}(\mathbf{x}(\mathbf{X}, t), t) = \mathbf{v}(\mathbf{X}, t)$.

The deformation of a body depends on the relative motion of neighboring particles, and can be characterized in a number of ways [15]. For our purposes, we will describe the relationship between velocities at neighboring points with the rate of deformation tensor (or rate of strain tensor)

$$\mathbf{D} = \left[\begin{array}{cc} u_x & \frac{1}{2}\{u_y + v_x\} \\ \frac{1}{2}\{u_y + v_x\} & v_y \end{array} \right]$$

$\mathbf{D}$ corresponds to the symmetric part of the velocity gradient tensor $\mathbf{L}$. The antisymmetric part is called the vorticity tensor $\mathbf{W}$. In our analysis of the deformable motion we assume that the rate of deformation tensor and the vorticity tensor are locally homogeneous. However we note that $\mathbf{D}$ and $\mathbf{W}$ will change from one neighborhood of the myocardium to another. Similar assumptions in the biomechanical literature have assumed that the deformation gradient tensor in the myocardium was locally homogeneous [8]. We can perform a local analysis of the Eulerian velocity field. Let $\mathbf{x}$ be a point in the deformed body. For any point $\mathbf{x} + \delta\mathbf{x}$ in a small neighborhood around $\mathbf{x}$ we have

$$\mathbf{u}(\mathbf{x} + \delta\mathbf{x}, t) = \mathbf{u}(\mathbf{x}, t) + \mathbf{L}\delta\mathbf{x} \tag{1}$$

The physical assumption of local homogeneity of rate of deformation results in the locally linear (or affine) model (1). This model appears to be a good tradeoff between the exhaustive description of the entire set of noisy observed velocities, and a crude model of the velocity, which would assume a constant motion inside each cell. Furthermore this model allows us to estimate the rate of deformation, an essential parameter in the analysis of the myocardial deformation.

Let Δ be the mesh associated with the triangulation of the myocardium. Let N be the number of nodes of the partition. We consider now the space P_Δ^0 of continuous piecewise polynomial functions in two arguments and of degree one. A local basis of P_Δ^0 is composed of the collection $(\xi_k)_{k=1...N}$, where ξ_k is the linear function which takes the value 1 at the vertex k and vanishes on all other nodes (see Figure 1a). The basis $(\xi_k)_{k=1...N}$ is not orthogonal but the product $\int_\Delta \xi_k \xi_j$ is equal to zero each time that the nodes k and j are not in the same triangle. We can now express our model of the entire velocity field inside the myocardium. Inside each triangle the velocity is described by the linear model (1). Across the boundaries the velocity is continuous. Each component of the velocity is thus a function of

P_Δ^0, and it can be expanded in the local basis $(\xi_k)_{k=1...N}$. We have

$$(u, v)(t) = \left(\sum_{k=1}^{N} u_k \xi_k, \sum_{k=1}^{N} v_k \xi_k \right)(t) \tag{2}$$

The advantage of this local basis is that the entire velocity field is completely described by the value of the velocity at each vertex of the triangulation. This important result sets up a one-to-one correspondence between the dense motion of the material points inside the medium, and the motion of the nodes of the mesh. We note that we are not working with a fixed grid, but rather with a deforming mesh that follows the myocardium. Therefore the position of the support of the function ξ_k will change at each instant. At any given instant t the state of the myocardium is uniquely described by the position $(x_i, y_i)(t)$, and the velocity $(u_i, v_i)(t)$ of each vortex of the partition. Our aim is to generate the best estimates of the sequence of $(x_i, y_i)(t)$ and $(u_i, v_i)(t)$, $i = 1, \ldots, N$ over the heart cycle, given observations of the velocity and of the position.

3. Position and velocity measurements

3.1. VELOCITY MEASUREMENTS

Velocity fields obtained from optical-flow method tend to be noisy. Velocity fields obtained from phase-contrast measurements are visually smoother but yield significant outliers on regions near the boundary of the myocardium, as shown in figure 1b. A general framework for locally regularizing the velocity field has been developed. The global vector field is approximated locally by continuous linear piecewise vector fields. Furthermore the approximation will be continuous across the common boundary of two cells. This model yields a local description of the velocities with a small number of crucial parameters.

Given an observation of the velocity field $\mathbf{u} = (u, v)$, our goal is to estimate the best approximation, $\mathbf{p} = (p, q)$ of $\mathbf{u}$ in $P_\Delta^0 \times P_\Delta^0$ that minimizes the error

$$< \mathbf{p} - \mathbf{u}, \mathbf{p} - \mathbf{u} >= \int_\Delta (\mathbf{p} - \mathbf{u})^2 = \int_\Delta (p - u)^2 + \int_\Delta (q - v)^2 \tag{3}$$

The two terms $\int_\Delta (p - u)^2$ and $\int_\Delta (q - v)^2$ are independent and can be minimized independently. Therefore we need only to solve the problem

$$\min_{p \in P_\Delta^0} \int_\Delta (p - u)^2 \tag{4}$$

where u is a one scalar function. Let $\boldsymbol{\alpha}$ be the coordinates of the expansion of p in the local basis $(\xi_k)_{k=1...N}$. The problem (4) can be expressed as

$$\min_{\alpha_i \in \mathbb{R}^N} \int_\Delta \left(\sum_{i=1}^N \alpha_i \xi_i - u \right)^2 \tag{5}$$

(5) is a classic least-squares problem. Taking the partial derivative with respect to α_i, the solution $\boldsymbol{\alpha}$ of (5) is given by the normal equations

$$\mathbf{A}\boldsymbol{\alpha} = \mathbf{r} \tag{6}$$

where $A_{ij} =< \xi_i, \xi_j >, i, j = 1, \ldots, N$, and $r_i =< \xi_i, u > i = 1, \ldots, N$. As mentioned before, (ξ_i) is a local basis, and most of the inner products A_{ij} vanish to zero. There exists a very effective way to compute the matrix $\mathbf{A}$ and the vector $\mathbf{r}$ [2]. Again we note that the approximation method naturally extends to the 3-D case, although here, instead of solving two independent approximation problems, three problems need to be solved. Figure 1b shows the phase contrast velocity field in a small region around the myocardium. We note the turbulent flow in the blood pool, and the noisy vectors outside in the pericardial space. Figure 1c shows the result of the approximation algorithm. While keeping the same pattern and structure, the flow field is smoother. Noisy vectors have been discarded. This smooth velocity field can now serve as the input of our tracking algorithm.

The quality of the triangulation has a major influence on the accuracy of the approximation. On the one hand, triangles should be small to yield an accurate approximation of the velocity, and an accurate approximation of the contour. On the other hand, the number of points inside each triangle needs to be sufficient to estimate the parameters of the local affine model. We did not investigate here the problem of finding the best triangulation with respect to these two conflicting goals. We have developed an automatic 2-D triangulation scheme that exploits the shape particular to the left ventricle [11].

3.2. POSITION MEASUREMENTS

At each instant the contours of the epicardium and of the endocardium have been obtained using the deformable boundary/region growing approach presented in [3]. We update the position of the vertices of the triangulation that correspond to points on the boundaries of the myocardium. Our analysis exploits the prediction of the mesh position generated by the filter. Provided the dynamic model of the myocardial deformation is accurate, the position of a given material point at the next instant should lie in a small neighborhood around the predicted position. We project the prediction, $(x, y)(t + \delta t | t)$ onto the boundary $\partial \mathcal{B}(t + \delta t)$. The projection is defined
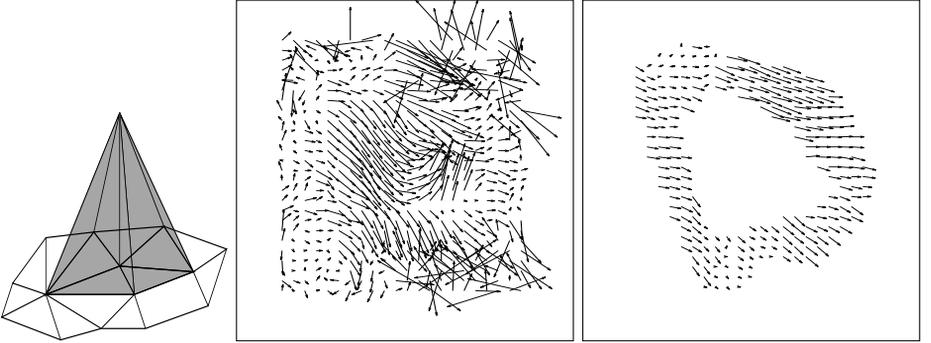
Figure 1. (a) The hat function ξ_k. (b) phase contrast MRI velocity field around the myocardium. (c) Continuous piecewise linear approximation of the velocity field shown in (b).

as the closest point from $(x, y)(t + \delta t|t)$ on $\partial \mathcal{B}(t + \delta t)$. As shown in the experiments, our algorithm does a very good job at predicting the position of the mesh at the next instant.

4. Tracking the partition

We assume that the vertices of the triangulation can be tracked independently. The assumption is realistic since we are tracking a deformable object, and we have independent position and velocity measurements for each node of the mesh. In order to obtain more tractable equations we simplify the Kalman filter and decouple the components x and y. We give in the following the equations for one of the components (x for instance).

We model the derivative of the Lagrangian velocity of each vertex as a sequence of zero-mean Gaussian noise. Let $\mathbf{x} = [x, \dot{x}]^T$ be the state vector that describes the x component of a given vertex of the mesh. We consider a discrete formulation of the problem where the discrete-time index k corresponds to $t + k\delta t$. The state vector evolves according to the following linear dynamic system

$$\mathbf{x}(k+1) = \mathbf{\Phi}\mathbf{x}(k) + \boldsymbol{\zeta}(k) \qquad \text{with} \qquad \mathbf{\Phi} = \begin{bmatrix} 1 & \delta t \\ 0 & 1 \end{bmatrix} \qquad (7)$$

where $\boldsymbol{\zeta}(k)$ is a two dimensional, zero mean Gaussian noise vector of covariance matrix $\mathbf{Q}(k)$. The above model provides only an approximation of the trajectory of the vertex over a short time interval. However, the noise $\boldsymbol{\zeta}(k)$ takes into account errors in the model and makes it possible to accommodate significant changes in velocity, as demonstrated in the experiments. From the position and the velocity measurements we can construct

the measurement vector $\mathbf{z}(k)$. The measurement system takes the form

$$\mathbf{z}(k) = \mathbf{x}(k) + \boldsymbol{\eta}(k) \tag{8}$$

where $\boldsymbol{\eta}$ is a two dimensional, zero mean Gaussian noise vector of covariance matrix $\mathbf{R}(k)$. Given the observations : $\mathbf{z}(1), \mathbf{z}(2), \ldots, \mathbf{z}(k)$, we wish to obtain an estimate of the state vector $\mathbf{x}$ at time k, $\mathbf{x}(k|k)$, which minimizes the mean-norm-squared-error. The optimal filtered estimate $\hat{\mathbf{x}}(k+1|k+1)$ can be efficiently computed with a recursive algorithm, the Kalman-Bucy filter [6]. We have

$$\hat{\mathbf{x}}(k+1|k+1) = \hat{\mathbf{x}}(k+1|k) + \mathbf{K}(k+1)\left[\mathbf{z}(k+1) - \hat{\mathbf{x}}(k+1|k)\right] \tag{9}$$

$$\hat{\mathbf{x}}(k+1|k) = \boldsymbol{\Phi}\mathbf{x}(k|k) \tag{10}$$

The gain matrix $\mathbf{K}(k+1)$ is given by

$$\mathbf{K}(k+1) = \mathbf{P}(k+1|k)^t \left[\mathbf{P}(k+1|k)^t + \mathbf{R}(k+1)\right]^{-1} \tag{11}$$

$\mathbf{P}(k+1|k)$ is the covariance matrix of $\hat{\mathbf{x}}(k+1|k)$. $\mathbf{P}(k+1|k+1)$ is the covariance matrix of $\hat{\mathbf{x}}(k+1|k+1)$. We have

$$\mathbf{P}(k+1|k) = \boldsymbol{\Phi}\mathbf{P}(k|k)\boldsymbol{\Phi}^t + \mathbf{Q}(k) \tag{12}$$

$$\mathbf{P}(k+1|k+1) = \left[\mathbf{I} - \mathbf{K}(k+1)\right]\mathbf{P}(k+1|k) \tag{13}$$

where $\mathbf{I}$ is the 2×2 identity matrix. Equation (9) consists in updating the prediction $\hat{\mathbf{x}}(k+1|k)$ with the new measurement $\mathbf{z}(k+1)$. The gain matrix $\mathbf{K}(k+1)$ controls the relative importance of the measurement with respect to the prediction. We note in (11) that if $\mathbf{R}(k+1)$, the covariance of the measurement, has very large components with respect to $\mathbf{P}(k+1|k)$, the covariance of the prediction, then $\mathbf{K}(k+1)$ is very small. Then $\hat{\mathbf{x}}(k+1|k+1)$ given by (9) essentially ignores the new measurement $\mathbf{z}(k+1)$, and is almost equal to the prediction. On the other hand if $\mathbf{R}(k+1)$ has very small components with respect to $\mathbf{P}(k+1|k)$, then $\mathbf{K}(k+1)$ is almost equal to $\mathbf{I}$, and $\hat{\mathbf{x}}(k+1|k+1)$ is almost equal to $\mathbf{z}(k+1)$. As explained by Gelb [6], the gain matrix is "proportional" to the uncertainty in the estimate, and "inversely proportional" to the measurements noise.

5. Experiments

We present here two experiments conducted with phase contrast MRI that best illustrate the approach. The protocol for the acquisition is fully described in [4]. In order to judge the accuracy of the trajectories obtained with our method we first present an experiment conducted with a phantom.

5.1. PHANTOM DATA

The phantom consisted of a gel-filled disk undergoing rotation and translation in the plane. The disk had four small markers on its outer edge which allowed to recover the rigid motion of the disk. The phantom was imaged in a quadrature head coil using cine PC gradient echo images sequence.

We have superimposed the result of the triangulation on a magnitude image in figure 2a. The trajectories of the marker were manually hand-traced. The trajectories of the nodes, and the trajectories of the markers are shown in figure 2b. The contours of the phantom at time 4 and at time 12 are also shown. The estimated trajectories are in close agreement with the trajectories of the markers. Our approach does not model the motion of the mesh as a periodic function. However, as shown in figure 2b almost all the trajectories are closed. This good result could clearly be improved by imposing a periodicity constraint as proposed in [9]. Figure 3a shows the piecewise linear approximation of the 2-D velocity field at time 9. We note that the approximation is smooth and accurately captures the complex pattern of the complete flow.

The quality of the prediction generated by the Kalman filter is illustrated in figure 3b. We have displayed the predicted positions of the nodes at time 10 and the real contours at time 9 and 10. For the clarity of the figure we have only displayed the inner contour. We note the accuracy of the prediction. This experiment validates the tracking algorithm in the case of complex rigid motion.

5.2. *IN VIVO* DATA

To further validate our approach with non-rigid motion the tracking algorithm has been tested with *in vivo* data. A dog was positioned in the quadrature head coil for MR imaging. The tracking started at time 13. Figure 5 shows the deformed mesh at time 1 (end-diastole), 5, 9 (end-systole), and 13. The piecewise linear velocity field is shown in figure 6 at the corresponding instants. Figure 4 shows the trajectory of the nodes attached to the endocardium. To help visualize the non-rigid motion of the endocardium, contours have been plotted at time 2, 6, 10 and 14. We first note that the tracking is stable and not perturbed by the flow inside the LV. Also, as mentioned previously the periodicity of the motion is not a priori modeled in the estimation problem. This explains why a few trajectories are not closed. However, given the significant gross motion of the heart (5 pixels from end-diastole to end-systole), the estimated trajectories are reasonable. These encouraging results should clearly be improved when the analysis will be performed in 3-D.

6. Conclusion

We have proposed a new unified framework to track the non-rigid motion of the myocardium using velocity maps and boundary information. The deformation of the myocardium is characterized by a deforming mesh. A general framework for locally regularizing the velocity field has been developed. The tracking is modeled as an estimation problem which makes it possible to properly take into account uncertainties in the velocity and boundary measurements. Results of experiments conducted on phantom data and on *in vivo* data demonstrate the strength of the approach. We are currently working on the 3-D extension of this work.

Acknowledgments

References

1. J.K. Aggarwal, Q. Cai, W. Liao, and B. Sabata. Articulated and elastic non-rigid motion: A review. In *Proc. IEEE Workshop on Motion of Non-Rigid and Articulated Objects, Austin, Texas, November 11-12*, pages 2–14, 1994.
2. E.B. Becker, G.F. Carey, and J.T. Oden. *Finite Elements, An Introduction, Volume I*. Prentice-Hall, 1981.
3. A. Chakraborty, L.H. Staib, and J.S. Duncan. Deformable boundary finding influenced by region homogeneity. In *Proc. of CVPR'94, Seattle, Washington*, pages 624–627, 1994.
4. R.T. Constable, K.M. Rath, A.J. Sinusas, and J.C. Gore. Development and evaluation of tracking algorithms for cardiac wall motion analysis using phase velocity MR imaging. *Magnetic Resonance in Medecine*, Vol. 32:33–42, 1994.
5. J.S. Duncan, R.L. Owen, L.H. Staib, and P. Anandan. Measurement of non-rigid motion using contour shape descriptors. In *Proc. Conference Computer Vision and Pattern Recognition, Hawaii*, pages 318–324, June 1991.
6. Arthur Gelb. *Applied Optimal Estimation*. MIT Press, 1974.
7. M.A. Guttman, J.L. Prince, and E.L. McVeigh. Tag and contour detection in tagged MR images of the left ventricule. *IEEE Trans. on Medical Imaging*, Vol. 13, No.1:74–88, March 1994.
8. A.D. McCulloch and J.H. Omens. Non-homogeneous analysis of three-dimensional transmural finite deformation in canine ventricular myocardium. *J. Biomechanics*, Vol. 24, No 7:pp 539–548, 1991.
9. J.C. McEachen, A. Nehorai, and J. Duncan. A recursive filter for temporal analysis of cardiac motion. In *Proc. IEEE Workshop on Biomedical Image Analysis, Seattle, Washington*, pages 124–133, 1994.
10. F.G. Meyer and P. Bouthemy. Region based tracking using affine motion models in long image sequences. *CVGIP: Image Understanding*, Vol. 60 No. 2:119–140, Sept. 1994.
11. F.G. Meyer, R. T. Constable, A. J. Sinusas, and J. S. Duncan. Tracking myocardial deformation using spatially-constrained velocities. Submitted to *IEEE on Medical*

Imaging, also available as Technical Report 951-1, 1995.

12. N.J. Pelc, R.J. Herfkens, and L.R. Pelc. 3-D analysis of myocardial motion and deformation with phase contrast cine MRI. In *Proc. of SMRM, 11th Annual Meeting, Berlin*, page 18, 1992.

13. P. Shi, A. Amini, G. Robinson, A. Sinusas, R.T. Constable, and J. Duncan. Shape-based 4-D left ventricular myocardial function analysis. In *Proc. IEEE Workshop on Biomedical Image Analysis, Seattle, Washington*, pages 88–97, 1994.

14. S.M. Song, R.M. Leahy, D.P. Boyd, B.H. Brundage, and S. Napel. Determining cardiac velocity fields and intraventicular pressure distribution from a sequence of ultrafast CT cardiac images. *IEEE Trans. on Medical Imaging*, Vol. 13, No.2:386–397, June 1994.

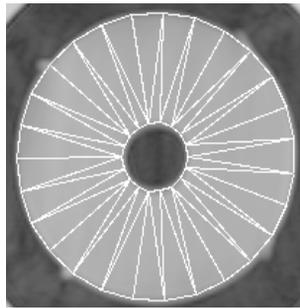15. A.J.M. Spencer. *Continuum Mechanics*. Longman, 1980.

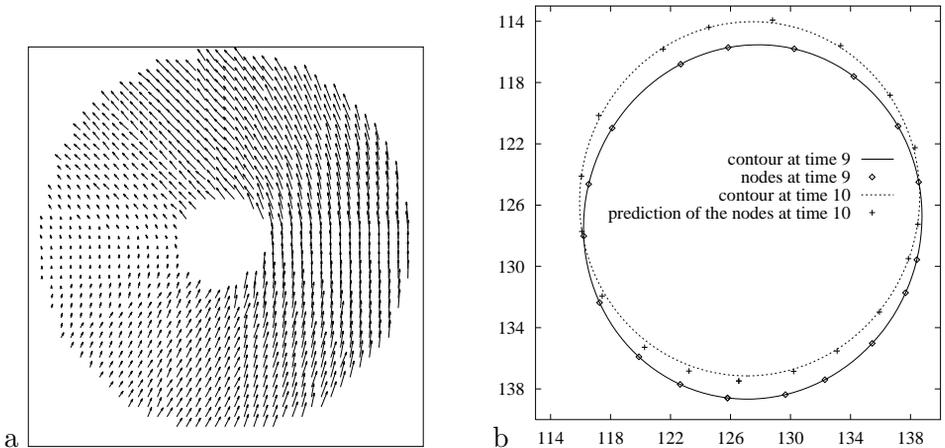*Figure 2.* Phantom at instant 0, with superimposed mesh.

Figure 3. (a) Piecewise linear flow field at time 9. (b) Prediction of the nodes on the inner contour at time 9. The actual contours at time 9 and 10 are shown to demonstrate the accuracy of the prediction.
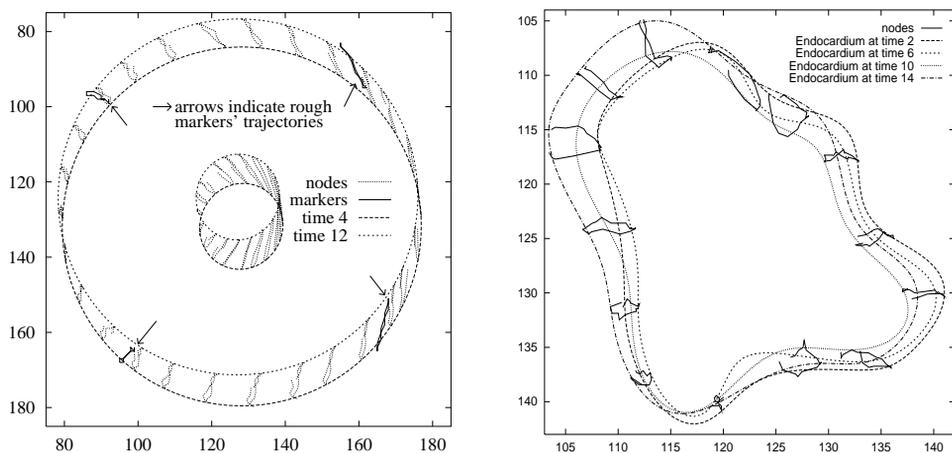
Figure 4. (a) Trajectories of the tracked nodes and trajectories of the hand-traced markers. The contours of the phantom are superimposed at time 4 and at time 12 only. (b) Trajectories of the nodes attached to the endocardium, with contours of the endocardium at time 2, 6, 10 and 14.
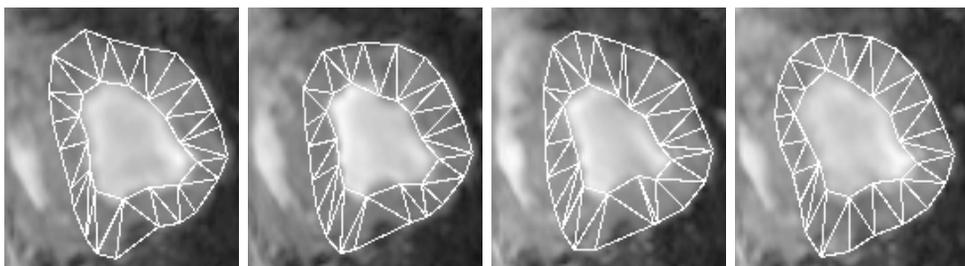

Figure 5. From left to right: results of the tracking at time 1 (end-diastole), 5, 9 (end-systole), and 13.
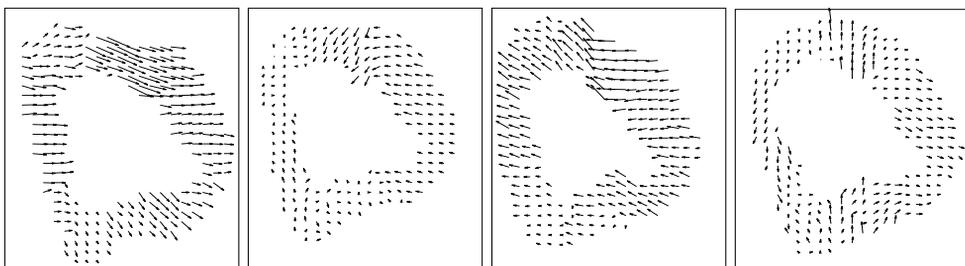

Figure 6. Continuous piecewise linear approximation of the velocity field at time 1, 5, 9, and 13.